

Field-free Josephson diode with controllable efficiency using magnetic tunnel barrier

Pramod. K. Sharma,¹ Sagnik Banerjee,² Biswajit Dutta,¹ Vansh Singhal,¹
Pushpak Banerjee,¹ Sonam Bhakat,¹ Hridis K. Pal,^{2,3} and Avradeep Pal^{*1,3}

¹*Department of Metallurgical Engineering and Materials Science,
Indian Institute of Technology Bombay, Powai, Mumbai 400076, India*

²*Department of Physics, Indian Institute of Technology Bombay, Powai, Mumbai 400076, India*

³*Centre of Excellence in Quantum Information, Computation, Science and Technology,
Indian Institute of Technology Bombay, Powai, Mumbai 400076, India*

Josephson diodes (JDs) offer a promising route towards realizing dissipation-less rectification at low temperatures. To be practically viable, a JD must operate at zero magnetic fields, exhibit high operating frequencies and efficiency, and possess tunability and scalability. In this study, we propose and experimentally demonstrate a straightforward mechanism that encompasses all these crucial features. Our approach involves utilizing an asymmetric Josephson junction with a magnetic weak link to attain a diode effect in the switching current. We substantiate this concept experimentally through the fabrication of mesa-type sputter-deposited tri-layered ferromagnetic long NbN/GdN/NbN Josephson junctions (JJs) in cross geometry. A robust zero-field diode effect is observed with an efficiency boost of up to 40% achievable through modification of the micromagnetic structure of the barrier. Notably, these diodes maintain high efficiency across a wide temperature range, from the lowest temperatures up to at least 4.2K, and exhibit an operating frequency of nearly 28GHz.

With the rise of quantum technologies, a growing need for non-dissipative diodes capable of operating at low temperatures is evident. Among the promising candidates JDs, which are JJs with non-reciprocal supercurrent, stand out. Recent years have witnessed intense theoretical [1–4], and experimental research in this direction. Initial attempts were largely based on magneto-chiral anisotropy [5–9], which require an external magnetic field for the desired effect (see also Ref. [10]). However, for practical applicability, a JD must operate at zero field. Various mechanisms were subsequently proposed and experimentally realized in the pursuit of this goal. These include inducing an out-of-plane polarization of weak link [11], engineering an effective ϕ_0 junction ground state [12], using the orbital magnetism in a twisted bilayer graphene JJ [13], employing a superconducting electrode with exotic order parameter symmetry [14], and artificially engineering Abrikosov vortices in long JJs [15].

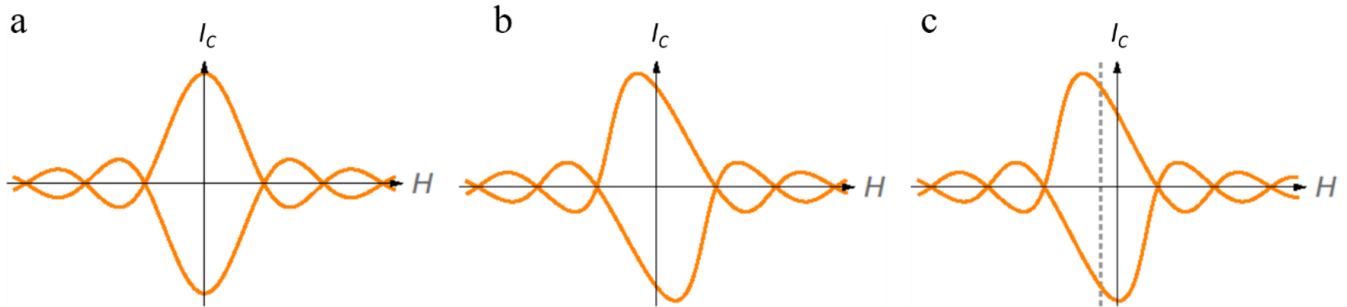


FIG. 1: a) Shows I_c vs H (Fraunhofer pattern) for non-magnetic short Josephson Junction, b) Fraunhofer pattern for a long Josephson Junction with asymmetric current injection, c) Fraunhofer pattern for a long Josephson Junction with asymmetric current injection and a magnetic barrier, showing broken mirror symmetry about $H = 0$.

The emergence of non-reciprocity in the JJ supercurrent invariably requires breaking of inversion and time-reversal symmetries. To achieve this at zero external field, much of the existing literature discussed above has taken recourse to exotic mechanisms at the microscopic level. Yet, an alternative approach exists which one can exploit at the macroscopic level to achieve the same objective. By manipulating the geometry of a JJ and using a magnetic weak link, both the inversion and time-reversal symmetries can be easily broken. Surprisingly, despite the apparent simplicity and viability of this avenue, there has been very little exploration in this direction. To the best of our knowledge, the only attempt towards realizing a non-reciprocal JJ using a magnetic weak link has been the study of

Josephson effect through single magnetic atoms of Cr and Mn [16]. Nevertheless, the diode effect in this work was achieved in the re-trapping current, which arises from the quasiparticles [3], instead of the switching current, which originates from the cooper pairs, and is, therefore, not dissipation-less.

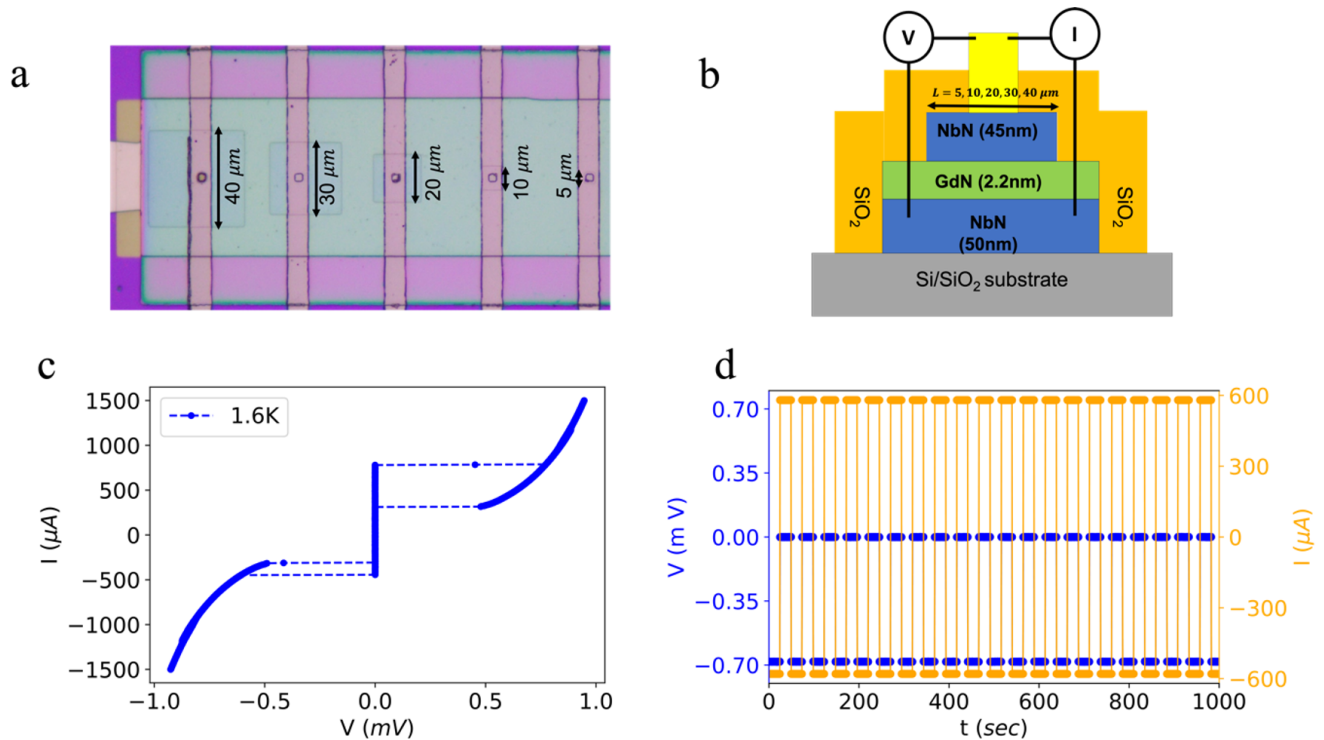


FIG. 2: a) Optical micrograph of the fabricated device, containing multiple Josephson Junctions of varying mesa areas, b) Schematic cross sectional view diagram of the measured Junctions showing the various layers and the measurement geometry, c) IV characteristics of the $1600 \mu\text{m}^2$ Junction, at just cooled state, d) Blue line represents half wave rectified voltage response of the Josephson junction diode at just cooled state, due to an applied square wave current signal (orange).

In this study, we propose and experimentally demonstrate for the first time a zero-field JD with pronounced switching current asymmetry using a weak magnetic link. We posit that any long JJ (a long JJ is defined as a JJ whose length L is larger than Josephson depth λ_J , i.e., $L > \lambda_J$) with a ferromagnetic barrier and a geometry that allows for asymmetric injection of current is inherently a zero-field JD, independent of any other material details. The origin of this effect can be understood as follows. A short ($L < \lambda_J$) nonmagnetic symmetric JJ (JJ with fabrication geometry that allows spatially symmetric current transmission, which is typical of an overlap JJ [17]) enjoys both time-reversal and inversion symmetries at the microscopic level, which guarantee reciprocity in the supercurrent. This is best reflected in the critical current I_c vs. the external field H curve, as shown schematically in Figure 1(a). The figure has reflection symmetries, both about the y and x axes, as well as the origin. These macroscopic symmetries may be thought of as effective manifestations of the underlying microscopic symmetries of the system. For nonreciprocity, these effective symmetries in the I_c vs H curve need to be broken. This is accomplished in our proposal in two steps. First, the reflection symmetry about the two axes is broken when a long asymmetric JJ is used in place of a short JJ [17–20]. As can be seen in Figure 1(b), the currents along opposite directions across the barrier, I_{c+} and I_{c-} , are no longer equal at nonzero H and the system acts as a diode. Nevertheless, the reflection symmetry about the origin is preserved and the reciprocity at zero field is still maintained. To break this, we next replace the nonmagnetic barrier with a ferromagnetic one. Shown schematically in Figure 1(c), the presence of an intrinsic magnetization in the barrier leads to a shift of origin which results in a diode effect even when the external field is zero. Explicit calculations supporting the above picture are presented in Supplementary Material (SM).

We now present an experimental realization of the idea espoused above using NbN/GdN/NbN spin-filter [21, 22] mesa-type long JJs in cross geometry, fabricated using a standard Nb/ AlO_x /Nb multi-step lithography process. An optical micrograph of the central device area with varying size mesas on top of a NbN ground line and wired with Nb cross bridges is shown in Figure 2(a), and a cartoon cross section of a junction is shown in Figure 2(b). In Figure 2(c)

we show the typical zero-field IV curve and demonstrate half-wave rectification of a square wave with a $40\ \mu\text{m} \times 40\ \mu\text{m}$ Josephson junction at 1.6K in Figure 2(d). The observed zero-field-diode efficiency $\eta = \frac{I_{c+} - I_{c-}}{I_{c+} + I_{c-}}$ is approximately 23%. This demonstrates that our JJ is, in fact, a JD as proposed. We note that these JDs have an $I_c R_n$ product of approximately $58\ \mu\text{V}$ (where I_c is defined as the highest magnitude of critical current of the junction and R_n is the normal state resistance of the junction) and an $R_n A$ product of approximately $67\ \Omega\ \mu\text{m}^2$ (where A is the junction area). The $I_c R_n$ value is greatly reduced in comparison to standard Nb/AIO_x/Nb SIS junctions on account of I_c suppression caused by a high degree of spin filtering arising due to the ferromagnetic insulating nature of the GdN barrier [21, 22]. The $R_n A$ product is in the range of what is expected of high-quality leakage-free Josephson tunnel barriers [23] and is close to previously reported values for NbN/ GdN/ NbN JJs [24]. The leak-free barrier quality can also be evinced from I_c approaching a zero value in the short junctions, observed with application of an in-plane magnetic field, and is discussed later in Figure 3. It must be noted, however, that for magnetic JJs, owing to barrier magnetisation and the accompanying hysteresis in I_c vs H , the highest I_c may not be occurring at zero external magnetic fields [22].

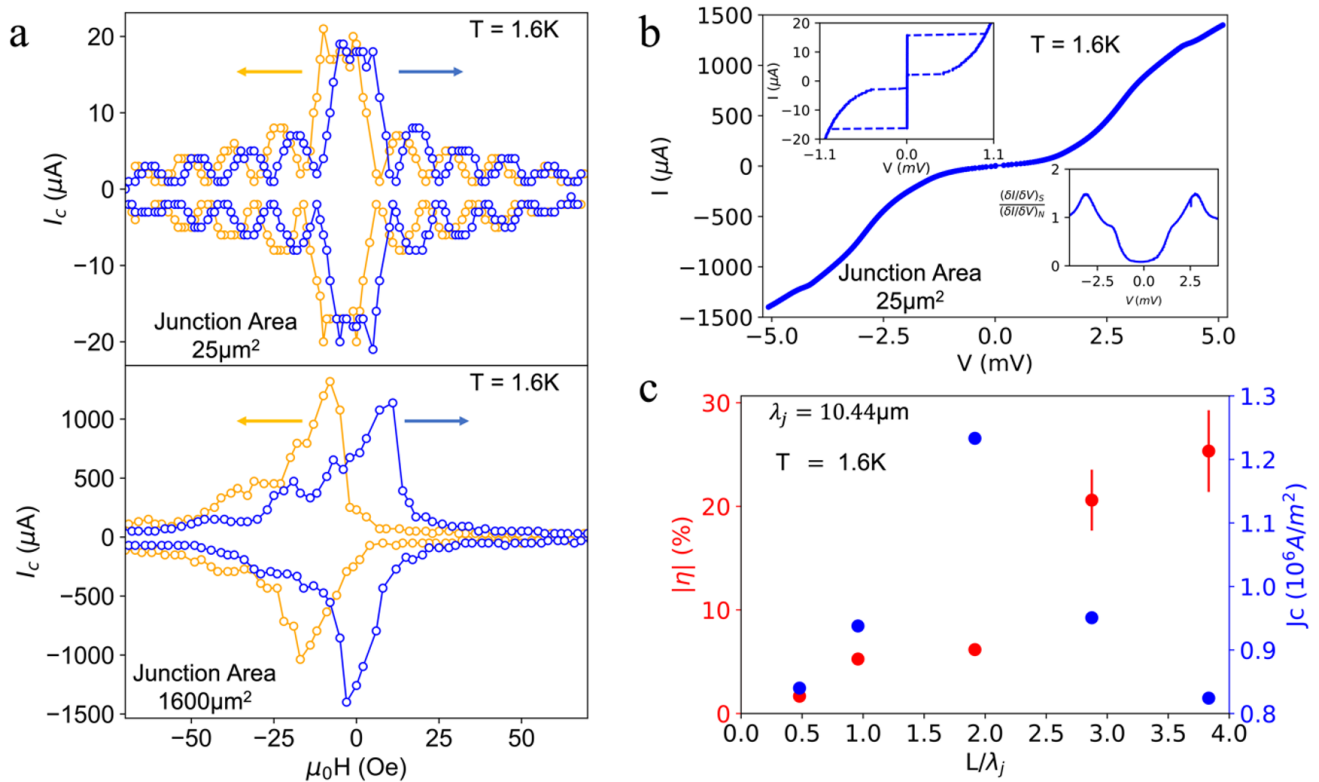


FIG. 3: a) Upper panel shows I_c vs H pattern obtained from $5\ \mu\text{m} \times 5\ \mu\text{m}$ short junction with hysteresis due to magnetic barrier. Lower panel shows I_c vs H pattern obtained from $40\ \mu\text{m} \times 40\ \mu\text{m}$ long junction. Blue open circles represent the field sequence in the positive direction, while orange open circles represent the field sequence in the negative direction, b) Blue open circles represent IV characteristic of the small junction and the inset shows the zoomed in region close to the critical current, c) Red circles denote the absolute diode efficiency plotted against the dimensionless parameter which is the ratio of junction length (L) to Josephson penetration depth (λ_J) and the blue circles represent the corresponding critical current density observed in these junctions.

As remarked earlier, three factors contribute to making a JD: a ferromagnetic barrier, asymmetric current injection, and junction length. In our devices ferromagnetic insulating GdN [25] provides the first aspect while the cross geometry provides the second. Keeping these two fixed, we have systematically investigated the third aspect—the length of the JJ. A single chip with several square shaped mesa type junctions was fabricated to demonstrate a gradual transition into non-reciprocal behaviour as we cross over from the regime of short junctions ($L/\lambda_J < 1$) to the regime of long junctions ($L/\lambda_J > 1$). In the upper panel of Figure 3(a), the I_c vs H of a $5\ \mu\text{m} \times 5\ \mu\text{m}$ JJ is shown, while in the lower panel the same is shown for a $40\ \mu\text{m} \times 40\ \mu\text{m}$ JJ (Josephson penetration depth $\lambda_J = \sqrt{\frac{\phi_0}{2\pi\mu_0 d' J_c}} = 10.44\ \mu\text{m}$ calculated using the critical current density J_c of the $5\ \mu\text{m} \times 5\ \mu\text{m}$ short junction). In the case of short junction, I_c

vs H hysteresis is observed as expected for a magnetic barrier [22]. In both these figures, the virgin curve (initial field ramp up from zero field to maximum positive field) has been omitted to demonstrate greater visual clarity regarding contrasting reciprocal and non-reciprocal behaviours for the short and long junctions. In Figure 3(c), we show the gradual evolution of η with increase in the degree of ‘longness’ of the JJs studied, where a largely monotonic increase from nearly zero to approximately 25% is observed. The data points are an average of several as-cooled zero field measurements, as well as zero field cooldowns after triangular ramp down demagnetisation procedures of the superconducting magnet from 50K - a temperature that is well above the Curie temperature of 35K for GdN. The error bars are representative of standard deviations of η across several such cooldowns.

The IV characteristic up to larger voltages beyond the superconducting gap voltage as well as their highly asymmetric differential conductance plots [26], is shown in Figure 3(b) to demonstrate the highly non-linear IV behaviour expected of SIS junctions. A zero field IV of the same junction with typical underdamped hysteretic reciprocal I_c behaviour is shown in the inset to Figure 3(b). It is evident that barring measurement accuracies, at all field values $I_{c+} = I_{c-}$, and no diode effect is observed either in switching current or in retrapping current.

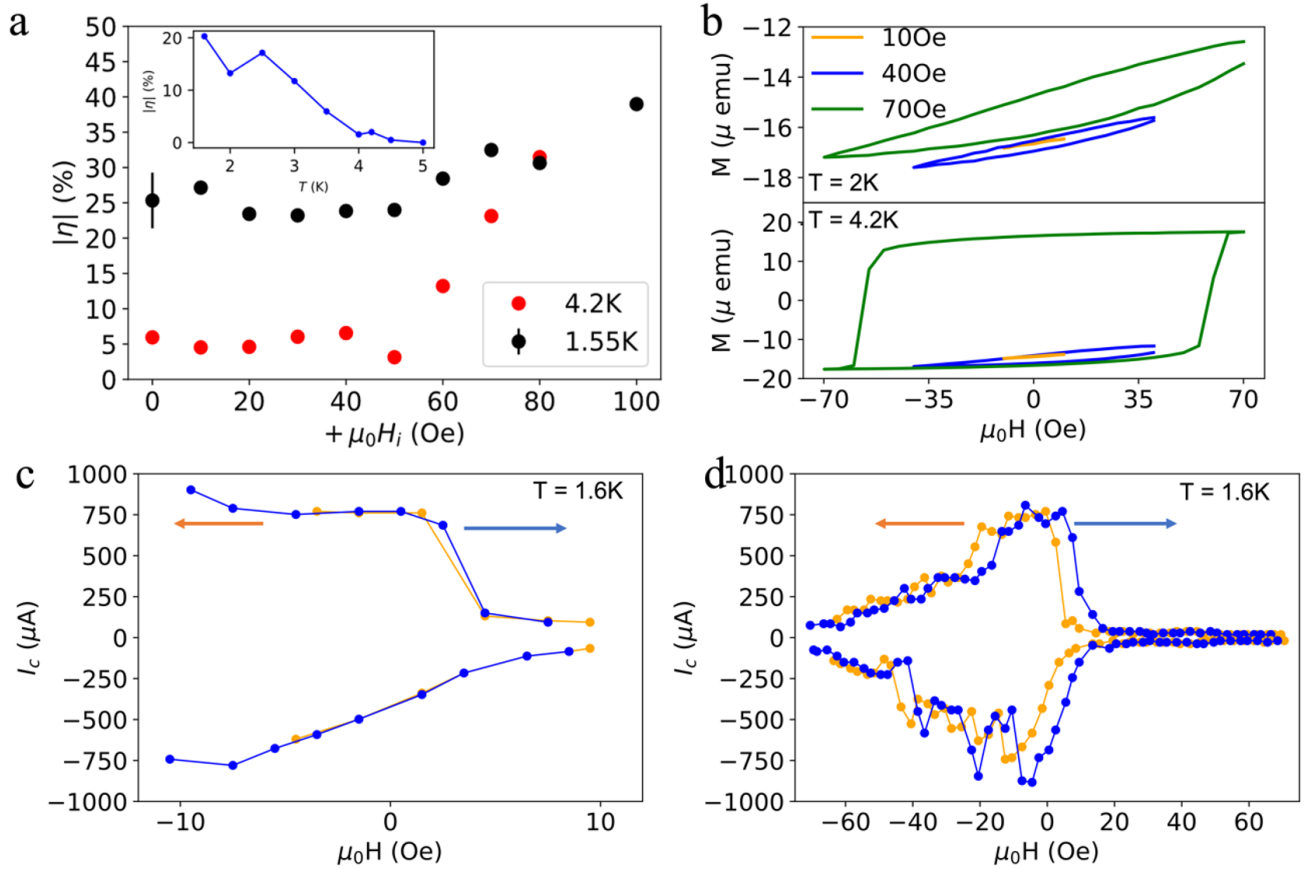


FIG. 4: a) Black circles denote the zero-field diode efficiency at 1.55K after completing one field cycle with an amplitude of H_i ($i = 1, 2, \dots, n$). Similarly, red circles mark efficiencies at 4.2K, b) M vs H for field ranges 10 Oe (orange), 40 Oe (blue), 70 Oe (green) at 2K and 4.2K, c) I_c vs H at 1.6K in the range ± 10 Oe, d) I_c vs H at 1.6K in the range ± 70 Oe.

Since domain structure is inherent in any ferromagnet, it is natural to ask if such a structure plays any role in the zero-field diode effect. The magnetic microstructure of the ferromagnet can be controlled through minor-loop cycling: Starting from zero field, we go to a field $-H_i$, followed by a ramp to $+H_i$, and then come back to zero field. The IV curve is then recorded at zero field following this process. This procedure is repeated for gradually increasing values of the field cycling amplitudes H_i , ranging from 0 Oe to 100 Oe. The resulting efficiency values at two different temperatures, 1.6K and 4.2K, are presented in Figure 4(a) (note that the η values for $H_i = 0$ in Figure 4(a) is the same as that used in Figure 3(c). All data correspond to the $40 \mu\text{m} \times 40 \mu\text{m}$ junction). The plot has two salient features. First, at both temperatures, the efficiency stays relatively unchanged up to a certain value of H_i and then increases monotonically. Second, at a given value of H_i , the efficiency is higher at lower temperatures.

To gain further insight into the appearance of these features, we measure the M - H minor loops of GdN in an unpatterned AlN/3 nm GdN/AlN sample at both 1.55K and 4.2K. This is shown in Figure 4(b). The corresponding I_c vs H curves in our JD at 1.55K are shown in Figs. 4(c) and 4(d) for two values of the field cycling amplitudes. In both cases the appearance of hysteresis sets in at similar values of the field cycling amplitude, giving us confidence that there is not much of a qualitative difference in magnetic microstructures between a large area GdN film and the GdN present in patterned junctions. Therefore, the former can be used as a proxy for the latter as regards the magnetic microstructure. With this set, we now compare Fig. 4(a) with Fig. 4(b). We observe that the uptrend in the efficiency at both temperatures in Fig. 4(a) directly correlates with the appearance of a visible hysteresis in the corresponding $M - H$ minor loops in Fig. 4(b). This directly points to the importance of the microstructure of the ferromagnet in determining the efficiency of the diode effect.

We next focus on the decrease of zero-field η with temperature (approximately 25% at 1.55K to approximately 5% at 4.2K). A monotonically decreasing trend is observed as shown in the inset to Figure 4(a). The critical current density at 4.2K is marginally lower as compared to 1.55K (refer to SM for temperature dependence of critical current), and hence a temperature-dependent increase in λ_J can be ruled out as a probable cause for this observation. It is well known that there is a large change in anisotropy and switching field of GdN below 5K [27]. Hence it can be speculated that the overall softer nature of the ferromagnet (and therefore a difference in domain structure) is a major contributor to the observed increasing diode efficiency with a lowering of temperature. Further theoretical work is necessary to fully explain the above-observed effects.

The above findings provide unambiguous evidence that the efficiency of the JD is also intricately dependent on the magnetic microstructure, in addition to the overall magnetization due to the magnet. This, in turn, furnishes us with an additional means to manipulate and enhance the tunability of zero-field efficiency in our junctions—an aspect that can be fruitfully exploited in practical applications conclusion, by using a novel approach of breaking the symmetry in I_c vs H Fraunhofer patterns through the usage of long magnetic JJs in cross geometry, we have demonstrated a very reliable and reproducible JD where the degree of non-reciprocity can be tuned by manipulating the micromagnetic structure. This JD is operable up to at least 4.2K and has a high operational frequency of approximately 28GHz. The growth and fabrication of such junctions are achieved using standard industrially adopted Nb fabrication technology processes. The zero-field efficiency and operational frequency of such JDs can be engineered by varying multiple parameters including the magnetization of the barrier material and the critical current density through thickness changes of the magnetic barrier; by changing the junction dimensions; incorporating other magnetic barriers etc. This paves a new pathway to the realization of JDs and opens up possibilities of engineering the diode effect. This demonstration of efficient, tunable, fast, and field-free non-reciprocal Josephson transport, achieved through industrially viable methods like multi-layer sputtering and multi-stage optical lithography, marks a significant advancement in Josephson diode technology.

Acknowledgements

The work was financially supported by a grant from National Supercomputing Mission, India under Grant Number - DST/NSM/R&D Exascale/2021/10.

Methods

Multilayer Growth: Si/SiO₂ substrate is used for the growth of NbN/GdN/NbN stack. All deposition were done in custom custom-designed ultra-high-vacuum sputter system with 5 magnetron sources capable of with a base pressure lower than 2×10^{-9} mbar. DC reactive magnetron sputtering was done to deposit both NbN and GdN from Nb and Gd targets, in Ar atmosphere containing 28% N₂ and 8% N₂ respectively. All layers were deposited, without breaking the vacuum, in order to produce high-quality interfaces. The bottom layer NbN thickness is 50nm, GdN thickness is 2.2nm, top layer NbN thickness is 45nm.

Fabrication of Josephson junctions: Sputter-grown multi-layers were further processed to produce the mesa-type Josephson Junctions. Multi-stage photolithography was performed using MJB6 (Karl Suss) and micro-writer ML3 (Quantum Design). NbN was etched using CF₄, and GdN was milled away using Ar-ion milling. A layer of 400nm SiO₂ was deposited on the top of the Junction area to create an isolation between top and bottom layers of NbN. A window of $3 \mu\text{m} \times 3 \mu\text{m}$ is defined in the SiO₂ layer on top of NbN mesa for facilitating a superconducting contact with an Nb cross bridge. Before the deposition of Nb contacts, mild Ar-ion milling was done to clean the surface of top NbN. Approximately 400nm of Nb was deposited for the cross bridge and lifted off as the final step.

Measurement of Josephson junctions: Transport measurements were performed in an Oxford TeslatonPT closed cycle refrigerator with a 12T superconducting magnet. To reduce the channel noise, custom made inline low-pass (8Hz) filters were installed on-board the PCB. The QCODES python environment was used for data collection. For IV and I_c vs H measurements, the current was sourced from NI PXIe-4322 Analog Output module, and the Junction Voltage was acquired using Keithley DMM6500. A voltage criterion was applied for collecting the critical current data. For the differential conductance dI/dV measurements, AC (331.33Hz) and DC signals were superimposed using a custom-made summing amplifier, and fed to the sample loaded atop a separate non-filtered PCB. The total voltage response of the sample was received by both Keithley DMM6500 (junction DC voltage) and DSP 7265 Lock-in amplifier. The differential resistance was collected from the lock-in R values.

Magnetisation measurements: All the magnetisation measurements were performed using SQUID vibrating-sample-magnetometer, M/S Quantum design. Dimension of the un-patterned GdN sample was 4mmx2mm and thickness 3nm. Measurement was done in isothermal mode where the magnetic field was applied parallel to the plane of the sample.

Supplementary Material

I. THEORY OF DIODE EFFECT IN A FERROMAGNETIC LONG JOSEPHSON JUNCTION WITH ASYMMETRIC INJECTION OF CURRENT

Our main proposal to achieve a diode effect, as stated in the main text, is to use a ferromagnetic long Josephson junction with an asymmetric injection of current. In this section, we substantiate this claim through explicit calculations.

The classic problem of the variation of current in Josephson junctions subjected to a homogeneous magnetic field has been studied extensively, both numerically and analytically. Here, we extend it to the case where the barrier is a single-domain ferromagnetic insulator of uniform magnetization. We consider the setup presented in figure S1.

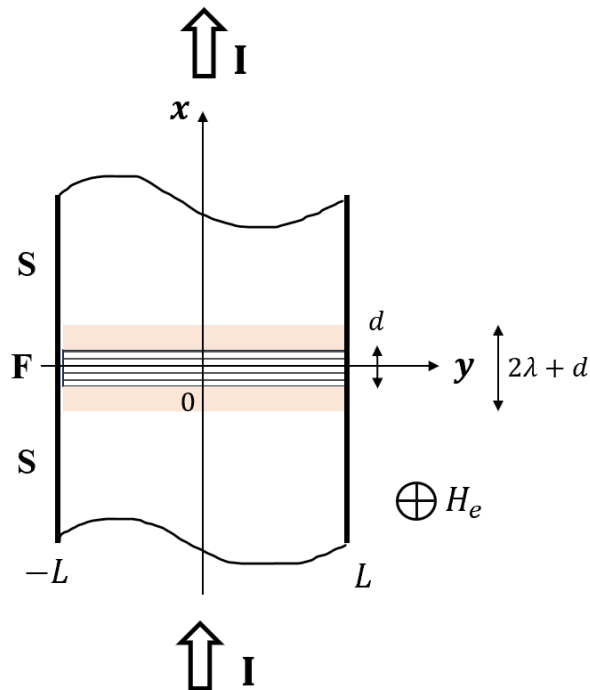


Figure S1: Schematic figure of a Josephson junction considered in this work: d is the thickness of the ferromagnetic material and λ is the London penetration depth of the superconductors. A homogeneous magnetic field H_e is directed into the plane of paper. The transport supercurrent I is along the x axis.

Two identical semi-infinite superconductors with breadth $W = 2L$ are placed with its faces parallel to the $y - z$ plane, at a separation d from each other. A ferromagnetic material of thickness d and length W is sandwiched between the faces of the superconductors. The x -axis lies perpendicular to the layering direction. A constant external homogeneous magnetic field H_e is applied along the z direction and the transport current I is injected along the x axis.

The dynamics of the system is specified by the gauge invariant phase difference $\phi(y)$ across the junction. The magnetic field at the junction has three contributions:

- i) The external field H_e
- ii) The induced field due to the Josephson current
- iii) Magnetization of the ferromagnet

Let $h(y)$ denote the resultant magnetic field due to (i) and (ii). $h(y)$ penetrates the junction in a region of width $d + 2\lambda$, λ being the London penetration depth of the superconductors. Consider an elemental rectangular region of dimensions $(d + 2\lambda)\Delta y$, at a distance y from the origin. The magnetic flux through the elemental region is (in

Gaussian units)

$$\Delta\varphi = h(y)(d + 2\lambda)\Delta y + 4\pi M d\Delta y, \quad (\text{S1})$$

where M is the magnetization. Note that M , in general, is a function of $h(y)$. For simplicity, in what follows, we assume that this is a constant (this suffices to understand the qualitative features of the experiment). The gauge invariant phase difference $\phi(y)$ across the junction is related to the flux $\Delta\varphi$ as [28]:

$$\Delta\phi = \frac{2\pi}{\phi_0}[h(y)(d + 2\lambda)\Delta y + 4\pi M d\Delta y], \quad (\text{S2})$$

where $\phi_0 = h/2e$ is the superconducting flux quantum. In the limit $\Delta y \rightarrow 0$:

$$\frac{d\phi}{dy} = \frac{2\pi}{\phi_0}[h(y)(d + 2\lambda) + 4\pi M d]. \quad (\text{S3})$$

Maxwell's equations relate the field $h(y)$ with the free current per unit length $j(y)$ as

$$\frac{dh}{dy} = \frac{4\pi}{c}j(y). \quad (\text{S4})$$

The current density $j(y)$ is related to the phase difference $\phi(y)$, following Josephson's current phase relation:

$$j(y) = j_1 \sin \phi. \quad (\text{S5})$$

Differentiating Eq. S3 and substituting Eqs. S4, S5 lead to the static Sine-Gordon equation:

$$\frac{d^2\phi}{dy^2} = \frac{1}{\lambda_J^2} \sin \phi, \quad (\text{S6})$$

where $\lambda_J = \sqrt{\frac{\phi_0 c}{8\pi^2 j_1 (d+2\lambda)}}$ is the Josephson penetration depth. Henceforth, we rescale $y \rightarrow y/\lambda_J$ and use $\hbar = c = 1$. Then, Eq. S6 becomes

$$\frac{d^2\phi}{dy^2} = \sin \phi. \quad (\text{S7})$$

To find the solution to the above equation, we need boundary conditions. To that effect, we use Eq. S3 at the endpoints:

$$\left. \frac{d\phi}{dy} \right|_L = \frac{2\pi}{\phi_0} \lambda_J [(2\lambda + d)h(L) + 4\pi M d], \quad (\text{S8})$$

$$\left. \frac{d\phi}{dy} \right|_{-L} = \frac{2\pi}{\phi_0} \lambda_J [(2\lambda + d)h(-L) + 4\pi M d]. \quad (\text{S9})$$

Integrating Eq. S4 along y , along with the continuity of the magnetic field at the junction edges yield the boundary conditions for the induced field $h(y)$, which can be written as [18]

$$h(L) + h(-L) = 2H_e, \quad (\text{S10})$$

$$h(L) - h(-L) = 4\pi I, \quad (\text{S11})$$

where $I = \int_{-L}^L dy j(y)$ is the total current flowing through the junction. Substitution of Eqs. S10 and S11 into Eqs. S8 and S9 leads to the expressions for H_e and I in terms of the phase derivatives at the boundary:

$$H_e = \frac{\phi_0}{4\pi\lambda_J(2\lambda + d)} \left[\left. \frac{d\phi}{dy} \right|_{+L} + \left. \frac{d\phi}{dy} \right|_{-L} \right] - H_0, \quad H_0 = \frac{4\pi M d}{2\lambda + d}, \quad (\text{S12})$$

$$I = \frac{\phi_0}{8\pi^2\lambda_J(2\lambda + d)} \left[\left. \frac{d\phi}{dy} \right|_{+L} - \left. \frac{d\phi}{dy} \right|_{-L} \right]. \quad (\text{S13})$$

So far, we have assumed that the junction is symmetric. However, in the experiment, the junction has a cross-type geometry. In this case, it is well known that there is an asymmetric current splitting at the junction edges and, as a result, the boundary conditions are modified as [17, 34],

$$H_e = \frac{\phi_0}{2\pi\lambda_J(2\lambda + d)} \left[a_+ \frac{d\phi}{dy} \Big|_L + a_- \frac{d\phi}{dy} \Big|_{-L} \right] - H_0, \quad (\text{S14})$$

$$I = \frac{\phi_0}{8\pi^2\lambda_J(2\lambda + d)} \left[\frac{d\phi}{dy} \Big|_L - \frac{d\phi}{dy} \Big|_{-L} \right], \quad (\text{S15})$$

$$a_{\pm} \geq 0, \quad a_+ + a_- = 1 \quad (\text{S16})$$

The parameters a_{\pm} measure the degree of the asymmetry in current injection at the two edges. We note, however, that the above boundary conditions are ill-posed since they are not sufficient for the uniqueness of a solution to the Sine-Gordon equation S7 [29]. As suggested in Refs. 19, 30, and 31 among all the solutions, only those that minimize a certain Gibbs free-energy functional are physically realizable. In what follows, we have also adopted the same strategy. Further details may be found in the above references. Thus, the problem of finding the current as a function of the external field reduces to solving Eq. S7 subject to the conditions S14 and S15. To that effect, we multiply both sides of Eq. S7 by $\frac{d\phi}{dy}$ and integrate to obtain,

$$\frac{1}{2} \left[\frac{d\phi}{dy} \right]^2 + \cos \phi = C, \quad -1 \leq C < \infty, \quad (\text{S17})$$

C being the constant of integration. The solutions are divided into two types, depending on the domain of C , and are expressed in terms of Jacobi elliptic functions:

Type I: $-1 \leq C \leq 1$.

$$\begin{aligned} \phi_{\pm}(y) &= (2n + 1)\pi \pm 2\sin^{-1}[k \operatorname{sn}(y - y_0, k)], \\ n \in \mathbb{Z}, \quad -K(k) \leq y_0 < K(k), \quad k^2 &\equiv \frac{1+C}{2}, \quad 0 \leq k \leq 1. \end{aligned}$$

Type II: $1 \leq C < \infty$.

$$\begin{aligned} \phi_{\pm}(y) &= (2n + 1)\pi \pm 2 \operatorname{am} \left(\frac{y - y_0}{k}, k \right), \\ -kK(k) \leq y_0 < kK(k), \quad k^2 &\equiv \frac{2}{1+C}, \quad 0 < k \leq 1. \end{aligned}$$

The functions $\operatorname{am} u$ and $\operatorname{sn} u$ are the Jacobi elliptic amplitude and elliptic sine respectively and $K(k)$ is the complete elliptic integral of the first kind:

$$K(k) = \int_0^{\pi/2} d\theta \frac{1}{\sqrt{1 - k^2 \sin^2 \theta}}.$$

The signs of $\phi(y)$ (ϕ_+ or ϕ_-), and the value of the constants k and y_0 are determined from the boundary conditions S14 and S15. For simplicity, let us restrict our analysis to the first quadrant ($I \geq 0$, $H_e + H_0 \geq 0$). The solutions can readily be generalised to the other quadrants.

Solutions of Type I. The physically stable solutions are:

$$\phi_s(y) = 2 \cos^{-1} \left[k \frac{\operatorname{cn}(y + \beta, k)}{\operatorname{dn}(y + \beta, k)} \right], \quad k \in [k_c, 1), \quad \beta \in [0, \beta_c] \quad (\text{S18})$$

Here cn and dn are the Jacobi elliptic cosine and delta amplitudes, respectively. The above-mentioned values for k and β denote their domains of stability. The boundary of the stability region for $k_c = k_c(L)$ is determined by the

relation [19]:

$$cn(L, k_c)[-E(L, k_c) + (1 - k_c^2)L] + (1 - k_c^2)sn(L, k_c)dn(L, k_c) = 0. \quad (\text{S19})$$

Here $E(\psi, k)$ is the incomplete elliptic integral of the first kind with amplitude ψ and modulus k . The stability boundary $\beta_c = \beta_c(k)$ is given by the solution to the following functional equation [19]:

$$\begin{aligned} & cn(L + \beta_c, k)cn(L - \beta_c, k)[-E(L + \beta_c, k) - E(L - \beta_c, k) + (1 - k^2)L] \\ & + (1 - k^2)[sn(L + \beta_c, k)cn(L - \beta_c, k)dn(L + \beta_c, k) \\ & + sn(L - \beta_c, k)cn(L + \beta_c, k)dn(L - \beta_c, k)] = 0, \quad k \in [k_c, 1]. \end{aligned}$$

Substituting equation S18 in the boundary conditions S14, S15 yields:

$$H_e + H_0 = \frac{\phi_0}{\pi\lambda_J(2\lambda + d)}k\sqrt{1 - k^2} \left[a_+ \frac{sn(L + \beta, k)}{dn(L + \beta, k)} - a_- \frac{sn(L - \beta, k)}{dn(L - \beta, k)} \right] \quad (\text{S20})$$

$$I = \frac{\phi_0}{4\pi^2\lambda_J(2\lambda + d)}k\sqrt{1 - k^2} \left[a_+ \frac{sn(L + \beta, k)}{dn(L + \beta, k)} + a_- \frac{sn(L - \beta, k)}{dn(L - \beta, k)} \right] \quad (\text{S21})$$

$$k \in [k_c, 1), \quad \beta \in [0, \beta_c] \quad (\text{S22})$$

Note that I corresponds to the critical current I_c if we set $\beta = \beta_c$ in the above equations. This gives the desired dependence of I_c with H_e .

Solutions of Type II. This class of solutions is further divided into two types, depending on the stability domains determined by k and α :

$$\phi_{pe}(y) = (p - 1)\pi + 2am \left(\frac{y}{k} + K(k) + \alpha, k \right), \quad \alpha \in [0, \alpha_c], \quad p = 2m \quad (m = 0, 1, \dots), \quad (\text{S23})$$

$$\phi_{po}(y) = p\pi + 2am \left(\frac{y}{k} + \alpha, k \right), \quad \alpha \in [0, \alpha_c], \quad p = 2m + 1 \quad (m = 0, 1, \dots). \quad (\text{S24})$$

The values of k for which the respective solutions are stable are indexed by the integer p as:

$$p = 0, \quad k \in (k_1, 1), \quad (\text{S25})$$

$$p = 1, 2, \dots, \quad k \in (k_{p+1}, k_p] \quad (\text{S26})$$

The points k_p , $p = 1, 2, \dots$ are the roots of the equations:

$$pk_p K(k_p) = L, \quad p = 1, 2, \dots \quad (\text{S27})$$

The boundaries of the stability regions $\alpha_c = \alpha_c(k)$ for equation S23 are given by [19]

$$\begin{aligned} & k^2 sn \left(\frac{L}{k} + \alpha_c, k \right) sn \left(\frac{L}{k} - \alpha_c, k \right) cn \left(\frac{L}{k} + \alpha_c, k \right) cn \left(\frac{L}{k} - \alpha_c, k \right) \left[E \left(\frac{L}{k} + \alpha_c, k \right) + E \left(\frac{L}{k} - \alpha_c, k \right) \right] \\ & + sn \left(\frac{L}{k} - \alpha_c, k \right) cn \left(\frac{L}{k} - \alpha_c, k \right) dn^3 \left(\frac{L}{k} + \alpha_c, k \right) + sn \left(\frac{L}{k} + \alpha_c, k \right) cn \left(\frac{L}{k} + \alpha_c, k \right) dn^3 \left(\frac{L}{k} - \alpha_c, k \right) = 0, \end{aligned}$$

and for equation S24 are given by [19]

$$\begin{aligned} & \frac{k^2}{1 - k^2} sn \left(\frac{L}{k} + \alpha_c, k \right) sn \left(\frac{L}{k} - \alpha_c, k \right) cn \left(\frac{L}{k} + \alpha_c, k \right) cn \left(\frac{L}{k} - \alpha_c, k \right) \\ & \times \left[E \left(\frac{L}{k} + \alpha_c, k \right) + E \left(\frac{L}{k} - \alpha_c, k \right) - k^2 \left[\frac{sn \left(\frac{L}{k} + \alpha_c, k \right) cn \left(\frac{L}{k} + \alpha_c, k \right)}{dn \left(\frac{L}{k} + \alpha_c, k \right)} + \frac{sn \left(\frac{L}{k} - \alpha_c, k \right) cn \left(\frac{L}{k} - \alpha_c, k \right)}{dn \left(\frac{L}{k} - \alpha_c, k \right)} \right] \right] \\ & - \frac{sn \left(\frac{L}{k} - \alpha_c, k \right) cn \left(\frac{L}{k} - \alpha_c, k \right)}{dn \left(\frac{L}{k} + \alpha_c, k \right)} - \frac{sn \left(\frac{L}{k} + \alpha_c, k \right) cn \left(\frac{L}{k} + \alpha_c, k \right)}{dn \left(\frac{L}{k} - \alpha_c, k \right)} = 0. \end{aligned}$$

Substituting Eq. S23 in S14 and S15, we have

$$H_e + H_0 = \frac{\phi_0}{\pi\lambda_J(2\lambda + d)} \frac{\sqrt{1-k^2}}{k} \left[a_+ dn^{-1} \left(\frac{L}{k} + \alpha_c, k \right) + a_- dn^{-1} \left(\frac{L}{k} - \alpha_c, k \right) \right] \quad (\text{S28})$$

$$I = \frac{\phi_0}{4\pi^2\lambda_J(2\lambda + d)} \frac{\sqrt{1-k^2}}{k} \left[a_+ dn^{-1} \left(\frac{L}{k} + \alpha_c, k \right) - a_- dn^{-1} \left(\frac{L}{k} - \alpha_c, k \right) \right] \quad (\text{S29})$$

$$\alpha \in [0, \alpha_c], \quad p = 2m, \quad m = (0, 1, \dots). \quad (\text{S30})$$

Similarly, substituting Eq. S24 in S14 and S15, we have:

$$H_e + H_0 = \frac{\phi_0}{\pi\lambda_J(2\lambda + d)} \frac{1}{k} \left[a_+ dn \left(\frac{L}{k} + \alpha_c, k \right) + a_- dn \left(\frac{L}{k} - \alpha_c, k \right) \right] \quad (\text{S31})$$

$$I = \frac{\phi_0}{4\pi^2\lambda_J(2\lambda + d)} \frac{1}{k} \left[a_+ dn \left(\frac{L}{k} + \alpha_c, k \right) - a_- dn \left(\frac{L}{k} - \alpha_c, k \right) \right] \quad (\text{S32})$$

$$\alpha \in [0, \alpha_c], \quad p = 2m + 1, \quad m = (0, 1, \dots) \quad (\text{S33})$$

The above two sets of expressions give a complete set of physically relevant solutions for H_e and I in the first quadrant ($H_e + H_0 \geq 0, I \geq 0$). The results can be readily extended to the other quadrants. The overall sign of the phase (choosing ϕ_+ or ϕ_-) is determined from the boundary conditions, and hence depends on which quadrant the values of $H_e + H_0$ and I reside. Further, note that changing $\alpha \rightarrow -\alpha$ or $\beta \rightarrow -\beta$ doesn't affect the stability conditions for both ϕ_s and ϕ_p . For a fixed $|H_e|$ and $|I|$, the solutions in the other quadrants are obtained through the use of the following symmetry relations:

1) $\mathbf{H}_e + \mathbf{H}_0 \leq \mathbf{0}, \mathbf{I} \geq \mathbf{0}$:

$$\phi_s, \beta \rightarrow \phi_s, -\beta, \quad \phi_p, \alpha \rightarrow -\phi_p, -\alpha \quad (\text{S34})$$

2) $\mathbf{H}_e + \mathbf{H}_0 \geq \mathbf{0}, \mathbf{I} \leq \mathbf{0}$:

$$\phi_s, \beta \rightarrow -\phi_s, -\beta, \quad \phi_p, \alpha \rightarrow \phi_p, -\alpha \quad (\text{S35})$$

3) $\mathbf{H}_e + \mathbf{H}_0 \leq \mathbf{0}, \mathbf{I} \leq \mathbf{0}$:

$$\phi_s, \beta \rightarrow -\phi_s, \beta, \quad \phi_p, \alpha \rightarrow -\phi_p, \alpha \quad (\text{S36})$$

We now plot the variation of critical current I_c vs the external field H_e for various cases.

Case 1: Fig. S2(a). A short junction ($L=0.2$) with symmetric current injection ($a_+ = a_- = 0.5$) and a non-magnetic barrier ($M = 0$).

Case 2: Fig. S2(b). A long junction ($L=2$) with symmetric current injection ($a_+ = a_- = 0.5$) and a non-magnetic barrier ($M = 0$).

Case 3: Fig. S2(c). A long junction ($L=2$) with symmetric current injection ($a_+ = a_- = 0.5$) and a magnetic barrier ($M \neq 0$).

Case 4: Fig. S2(d). A long junction ($L=2$) with asymmetric current injection ($a_+ \neq a_-$) and a magnetic barrier ($M \neq 0$).

It is seen that a diode effect at both zero and non-zero magnetic fields emerges only in Case 4, supporting our claim.

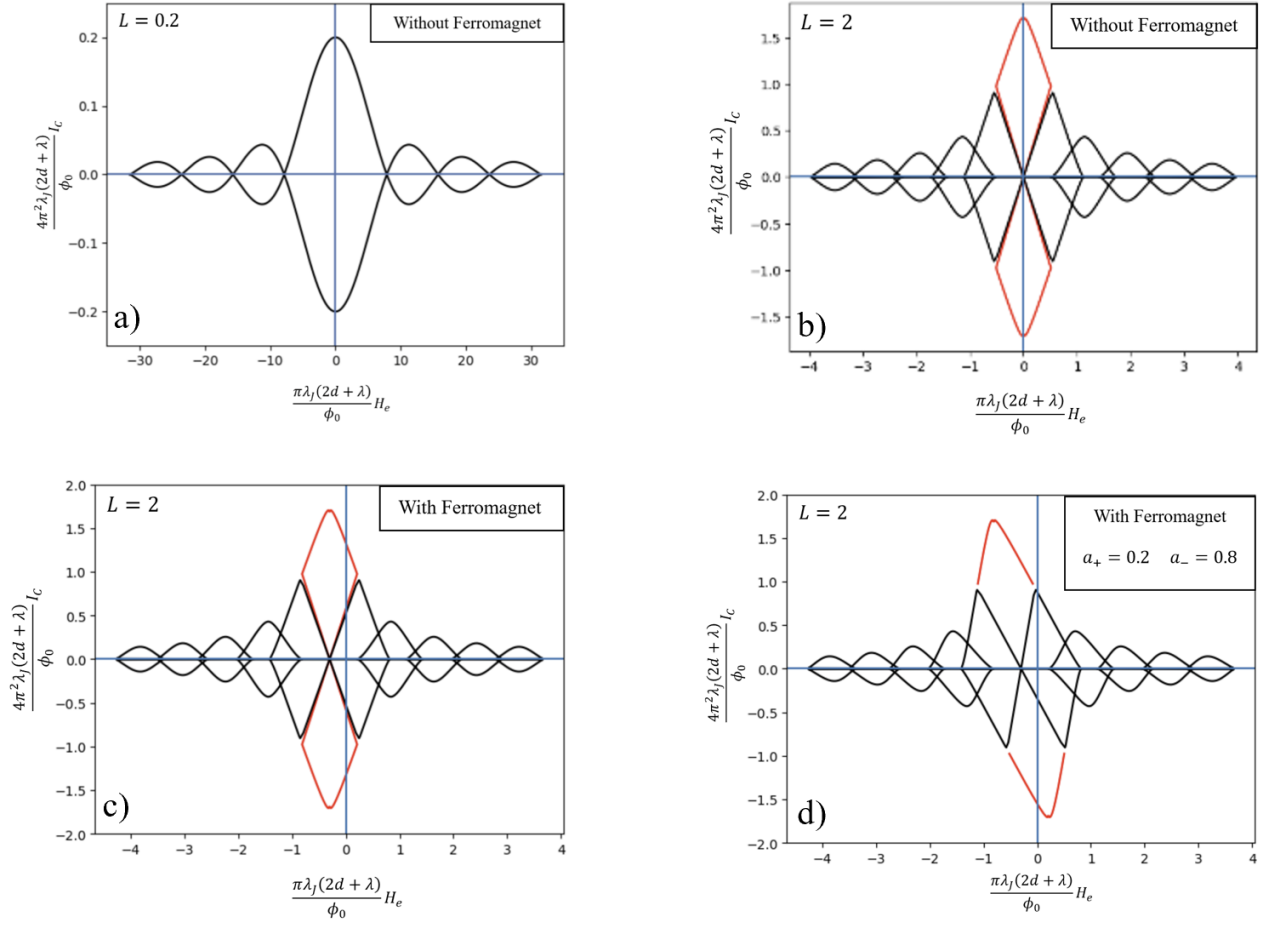


Figure S2: Variation of the critical current I_c with the external magnetic field H_e according to Eqs. S20, S21, S28, S29, S31 and S32 for a) A short junction ($L=0.2$) with symmetric current injection ($a_+ = a_- = 0.5$) and a nonmagnetic barrier; b) A long junction ($L=2$) with symmetric current injection ($a_+ = a_- = 0.5$) and a nonmagnetic barrier; c) A long ($L=2$) junction with symmetric current injection ($a_+ = a_- = 0.5$) and a ferromagnetic barrier—the ferromagnet is uniformly magnetized, with strength $H_0 = 0.3 \frac{\phi_0}{\pi \lambda_J (2d + \lambda)}$; d) A long ($L=2$) junction with asymmetric current injection ($a_+ = 0.2$, $a_- = 0.8$) and a ferromagnetic barrier with strength same as in (c). As can be seen, a non-reciprocal current emerges only in case (d), and this effect is present at all values of the field including zero. The red and black solid lines correspond to solutions of types *I* and *II*, respectively, as described in the text.

II. $M - H$ LOOPS OF GdN

MH loops of 3nm thick un-patterned GdN are shown in Fig. S3 at 2K and 4.2K. The saturation moment is $\sim 20\mu\text{emu}$. Coercive field is observed at $\sim 130\text{Oe}$ at 2K. As the temperature is increased coercive field is reduced to $\sim 70\text{Oe}$ at 4.2K.

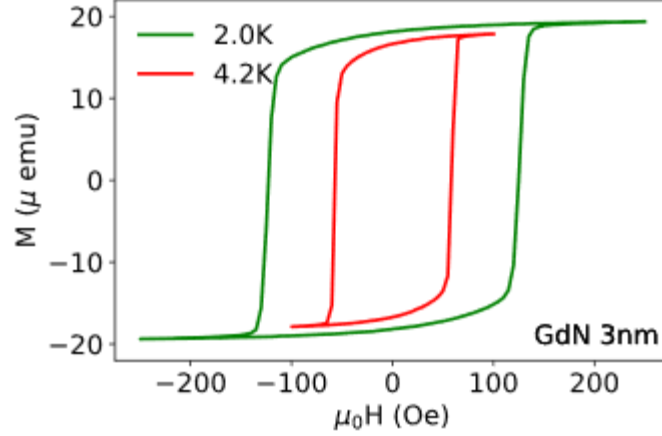


Figure S3: MH plot of 3nm thick un-patterned GdN recorded at 2K and 4.2K.

III. EFFICIENCIES AT ZERO AND NEAR-ZERO MAGNETIC FIELDS

I_c vs H of $40\mu\text{m} \times 40\mu\text{m}$ junction has been shown for $\pm 10\text{Oe}$ (Fig. S4a) and $\pm 70\text{Oe}$ (Fig. S4b) field range at 1.6K. The Josephson diode efficiency (η) is calculated at every point and shown by green stars. These plots clearly show the diode characteristic is present at zero applied field and as well as near the vicinity of zero field. For better visibility of efficiency (η) data has been shown $\pm 50\text{Oe}$ field range for Fig.S4b.

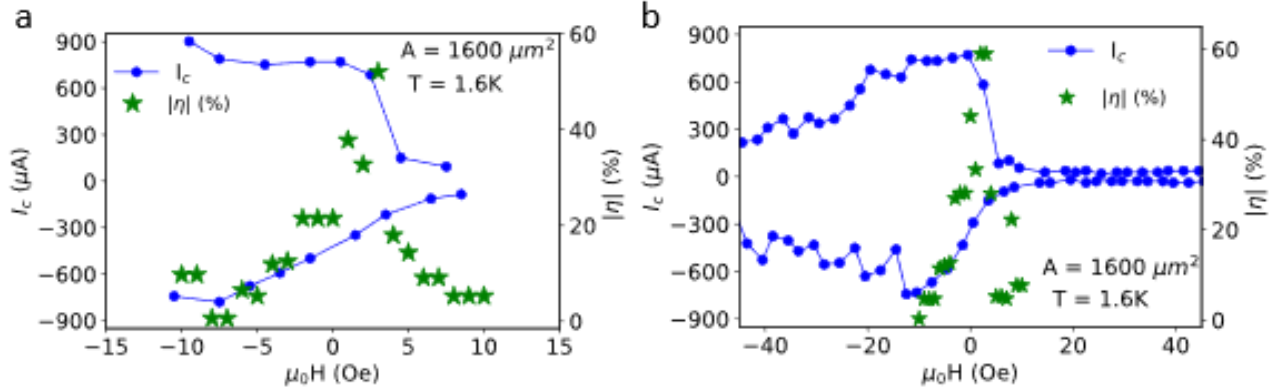


Figure S4: a) I_c vs H for field range $\pm 10\text{Oe}$ and, b) I_c vs H for field range $\pm 70\text{Oe}$. Efficiency at each point has been shown by green coloured stars.

IV. TEMPERATURE DEPENDENCE OF MAXIMUM CRITICAL CURRENT

The temperature dependence of maximum critical current of the long magnetic junction ($40\mu\text{m} \times 40\mu\text{m}$, GdN 2.2nm) is shown in Fig. S5. Due to hysteretic Fraunhofer, critical current maxima are not found at zero magnetic field. Critical current does not fall much till 6K, followed by a sharp drop. Since critical current does not fall much at 4.2K, junction is still in the long regime and shows non-reciprocal Josephson effect at 4.2K.

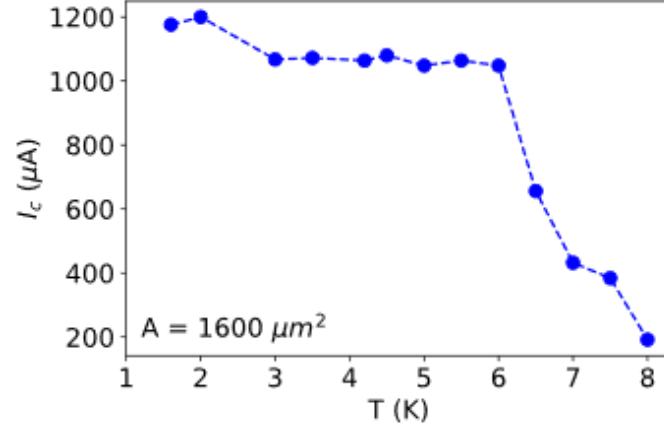


Figure S5: Dependence of I_c of a long junction of $40\mu\text{m} \times 40\mu\text{m}$ on temperature

V. EVOLUTION OF ZERO FIELD EFFICIENCY WITH CHANGING L/λ_j RATIO

Fig.S6 shows IV characteristic of the junctions of increasing dimension at as-cooled condition without exposing to the external field. As the ratio (L/λ_j) increases from 1 to 3, asymmetry evolves in I_{c+} and I_{c-} , resulting in non-reciprocal Josephson effect. IV plot for (L/λ_j) ~ 4 is shown in the main text of the manuscript.

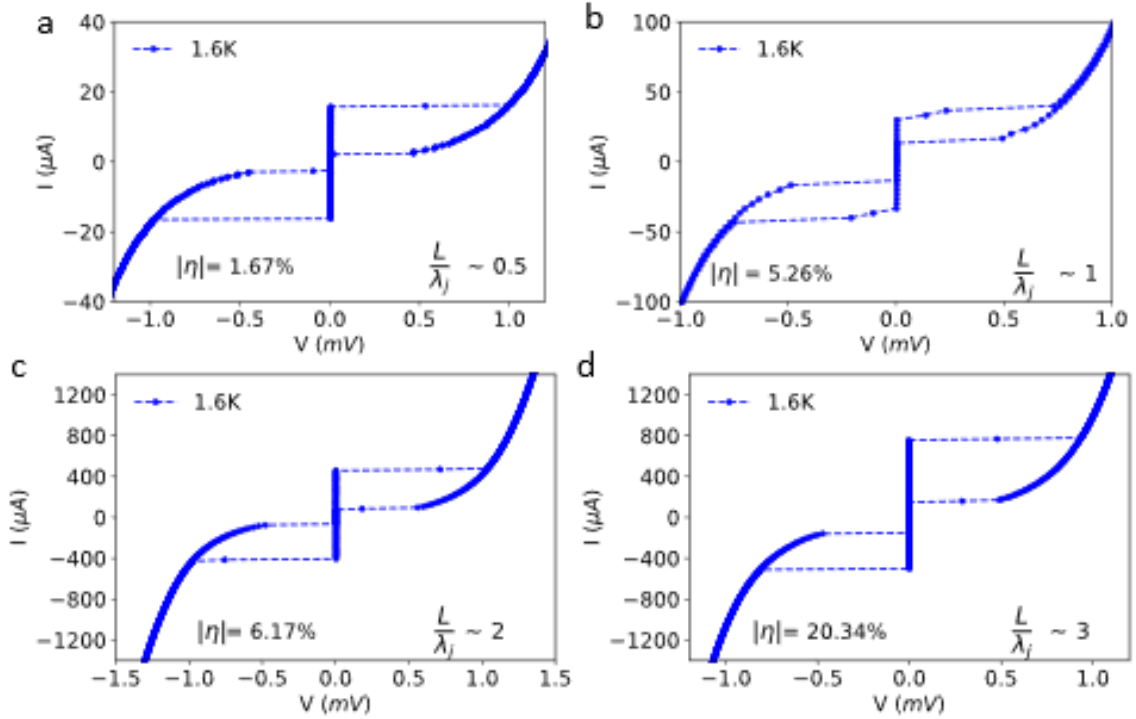


Figure S6: IV plot for different area junctions. a) and b) IV characteristic for $5\mu\text{m} \times 5\mu\text{m}$ and $10\mu\text{m} \times 10\mu\text{m}$ respectively, showing symmetrical I_{c+} and I_{c-} . c) and d) IV characteristic of $20\mu\text{m} \times 20\mu\text{m}$ and $30\mu\text{m} \times 30\mu\text{m}$ Junctions showing asymmetrical I_{c+} and I_{c-} .

[1] Yi Zhang, Yuhao Gu, Pengfei Li, Jiangping Hu, and Kun Jiang. General theory of josephson diodes. *Physical Review X*, 12(4):041013, 2022.

- [2] Margarita Davydova, Saranesh Prembabu, and Liang Fu. Universal josephson diode effect. *Science advances*, 8(23):eabo0309, 2022.
- [3] Jacob F Steiner, Larissa Melischek, Martina Trahms, Katharina J Franke, and Felix von Oppen. Diode effects in current-biased josephson junctions. *Physical Review Letters*, 130(17):177002, 2023.
- [4] Bo Lu, Satoshi Ikegaya, Pablo Burset, Yukio Tanaka, and Naoto Nagaosa. Tunable josephson diode effect on the surface of topological insulators. *Physical Review Letters*, 131(9):096001, 2023.
- [5] GLJA Rikken, J Fölling, and P Wyder. Electrical magnetochiral anisotropy. *Physical review letters*, 87(23):236602, 2001.
- [6] Fuyuki Ando, Yuta Miyasaka, Tian Li, Jun Ishizuka, Tomonori Arakawa, Yoichi Shiota, Takahiro Moriyama, Youichi Yanase, and Teruo Ono. Observation of superconducting diode effect. *Nature*, 584(7821):373–376, 2020.
- [7] Christian Baumgartner, Lorenz Fuchs, Andreas Costa, Simon Reinhardt, Sergei Gronin, Geoffrey C Gardner, Tyler Lindemann, Michael J Manfra, Paulo E Faria Junior, Denis Kochan, et al. Supercurrent rectification and magnetochiral effects in symmetric josephson junctions. *Nature nanotechnology*, 17(1):39–44, 2022.
- [8] Bianca Turini, Sedighe Salimian, Matteo Carrega, Andrea Iorio, Elia Strambini, Francesco Giazotto, Valentina Zannier, Lucia Sorba, and Stefan Heun. Josephson diode effect in high-mobility insb nanoflags. *Nano Letters*, 22(21):8502–8508, 2022.
- [9] Mohit Gupta, Gino V Graziano, Mihir Pendharkar, Jason T Dong, Connor P Dempsey, Chris Palmstrøm, and Vlad S Pribiag. Gate-tunable superconducting diode effect in a three-terminal josephson device. *Nature communications*, 14(1):3078, 2023.
- [10] Banabir Pal, Anirban Chakraborty, Pranava K Sivakumar, Margarita Davydova, Ajesh K Gopi, Avinandra K Pandeya, Jonas A Krieger, Yang Zhang, Mihir Date, Sailong Ju, et al. Josephson diode effect from cooper pair momentum in a topological semimetal. *Nature physics*, 18(10):1228–1233, 2022.
- [11] Heng Wu, Yaojia Wang, Yuanfeng Xu, Pranava K Sivakumar, Chris Pasco, Ulderico Filippozzi, Stuart SP Parkin, Yu-Jia Zeng, Tyrel McQueen, and Mazhar N Ali. The field-free josephson diode in a van der waals heterostructure. *Nature*, 604(7907):653–656, 2022.
- [12] Kun-Rok Jeon, Jae-Keun Kim, Jiho Yoon, Jae-Chun Jeon, Hyeon Han, Audrey Cottet, Takis Kontos, and Stuart SP Parkin. Zero-field polarity-reversible josephson supercurrent diodes enabled by a proximity-magnetized pt barrier. *Nature Materials*, 21(9):1008–1013, 2022.
- [13] J Díez-Mérida, A Díez-Carlón, SY Yang, Y-M Xie, X-J Gao, J Senior, K Watanabe, T Taniguchi, X Lu, Andrew P Higginbotham, et al. Symmetry-broken josephson junctions and superconducting diodes in magic-angle twisted bilayer graphene. *Nature Communications*, 14(1):2396, 2023.
- [14] Muhammad Shahbaz Anwar, Taketomo Nakamura, Ryosuke Ishiguro, Shafaq Arif, Jason WA Robinson, Shingo Yonezawa, Manfred Sigrist, and Yoshiteru Maeno. Spontaneous superconducting diode effect in non-magnetic nb/ru/sr2ruo4 topological junctions. *Communications Physics*, 6(1):290, 2023.
- [15] Taras Golod and Vladimir M Krasnov. Demonstration of a superconducting diode-with-memory, operational at zero magnetic field with switchable nonreciprocity. *Nature Communications*, 13(1):3658, 2022.
- [16] Martina Trahms, Larissa Melischek, Jacob F Steiner, Bharti Mahendru, Idan Tamir, Nils Bogdanoff, Olof Peters, Gaël Reece, Clemens B Winkelmann, Felix von Oppen, et al. Diode effect in josephson junctions with a single magnetic atom. *Nature*, 615(7953):628–633, 2023.
- [17] A Barone, WJ Johnson, and Ruggero Vaglio. Current flow in large josephson junctions. *Journal of Applied Physics*, 46(8):3628–3632, 1975.
- [18] CS Owen and DJ Scalapino. Vortex structure and critical currents in josephson junctions. *Physical Review*, 164(2):538, 1967.
- [19] SV Kuplevakhsy and AM Glukhov. Exact analytical solution of the problem of current-carrying states of the josephson junction in external magnetic fields. *Physical Review B*, 76(17):174515, 2007.
- [20] VM Krasnov, VA Oboznov, and Niels Falsig Pedersen. Fluxon dynamics in long josephson junctions in the presence of a temperature gradient or spatial nonuniformity. *Physical Review B*, 55(21):14486, 1997.
- [21] Kartik Senapati, Mark G Blamire, and Zoe H Barber. Spin-filter josephson junctions. *Nature materials*, 10(11):849–852, 2011.
- [22] Avradeep Pal, ZH Barber, JWA Robinson, and MG Blamire. Pure second harmonic current-phase relation in spin-filter josephson junctions. *Nature Communications*, 5(1):3340, 2014.
- [23] MS Goodchild, ZH Barber, and MG Blamire. Conductance and leakage in superconducting tunnel junctions. *Journal of Vacuum Science & Technology A: Vacuum, Surfaces, and Films*, 14(4):2427–2432, 1996.
- [24] Avradeep Pal, K Senapati, ZH Barber, and MG Blamire. Electric-field-dependent spin polarization in gdn spin filter tunnel junctions. *Advanced Materials*, 25(39):5581–5585, 2013.
- [25] MG Blamire, A Pal, ZH Barber, and Kartik Senapati. Spin filter superconducting tunnel junctions. In *Spintronics V*, volume 8461, pages 49–54. SPIE, 2012.
- [26] F Sebastian Bergeret, Alvise Verso, and Anatoly F Volkov. Spin-polarized josephson and quasiparticle currents in superconducting spin-filter tunnel junctions. *Physical Review B*, 86(6):060506, 2012.
- [27] Yi Zhu, Avradeep Pal, Mark G Blamire, and Zoe H Barber. Superconducting exchange coupling between ferromagnets. *Nature materials*, 16(2):195–199, 2017.
- [28] Michael Tinkham. *Introduction to superconductivity*. Courier Corporation, 2004.
- [29] R Courant and D Hilbert. *Methods of mathematical physics (interscience publ., new york and london)*, vol. 1. *vol*, 2:830, 1962.
- [30] SV Kuplevakhsy and AM Glukhov. Static solitons of the sine-gordon equation and equilibrium vortex structure in

- Josephson junctions. *Physical Review B*, 73(2):024513, 2006.
- [31] Sergey V Kuplevakhsy. Topological solitons of the Lawrence–Doniach model as equilibrium Josephson vortices in layered superconductors. *Low temperature physics*, 30(7):646–660, 2004.
- [32] Antonio Barone, Gianfranco Paterno, et al. *Physics and applications of the Josephson effect*. 1982.
- [33] Konstantin K Likharev. *Dynamics of Josephson junctions and circuits*. Routledge, 2022.
- [34] Ruggero Vaglio. Approximate analysis for stationary current flow in two-dimensional Josephson tunnel junctions. *Journal of Low Temperature Physics*, 25:299–315, 1976.